

## N O T I C E

THIS DOCUMENT HAS BEEN REPRODUCED FROM  
MICROFICHE. ALTHOUGH IT IS RECOGNIZED THAT  
CERTAIN PORTIONS ARE ILLEGIBLE, IT IS BEING RELEASED  
IN THE INTEREST OF MAKING AVAILABLE AS MUCH  
INFORMATION AS POSSIBLE

JPL PUBLICATION 81-8



# Application of Digital Image Processing Techniques to Astronomical Imagery 1980

Jean J. Lorre

(NASA-CR-164362) APPLICATION OF DIGITAL  
IMAGE PROCESSING TECHNIQUES TO ASTRONOMICAL  
IMAGERY 1980 (Jet Propulsion Lab.) 52 p  
HC A04/MF A01 CSCL 03A

N81-25006

63/89 Unclass  
42477

May 1, 1981

National Aeronautics and  
Space Administration

Jet Propulsion Laboratory  
California Institute of Technology  
Pasadena, California

JPL PUBLICATION 81-8

# Application of Digital Image Processing Techniques to Astronomical Imagery 1980

Jean J. Lorre

**ORIGINAL CONTAINS  
COLOR ILLUSTRATIONS**

May 1, 1981

National Aeronautics and  
Space Administration

**Jet Propulsion Laboratory**  
California Institute of Technology  
Pasadena, California

The research described in this publication was carried out by the Jet Propulsion Laboratory, California Institute of Technology, under contract with the National Aeronautics and Space Administration.

## PREFACE

The work described in this report was performed by the Observational Systems Division of the Jet Propulsion Laboratory.

## ACKNOWLEDGMENTS

The activities described in this report were encouraged by Dr. Edward Weiler at NASA Headquarters. Dr. Ray Wall, Manager of the Science Data Analysis Section which includes the Image Processing Laboratory, and Dr. Denis Elliott, Group Leader of the Astronomy Image Processing Group, were instrumental in supporting this project. I wish to thank Dr. Willem Wamsteker of the European Southern Observatory for his plates of M83; Dr. Allan Sandage of Mt. Wilson and Las Campanas Observatories for his plates of M82; Dr. Stephen Gull of Cavendish Laboratories, U.K. for the original maximum entropy algorithm; Dr. Mariaus Moles Villamate of Centro Astronomico Hispano-Aleman for his thoughts on new galaxy morphological classifications; and Dr. Alan Gillespie of JPL for his collaboration in the areas of illusions induced by properties of discrete digital images, a subject which still remains for the most part mysterious.

## ABSTRACT

Several areas of applications of image processing to astronomy have been addressed in this report. These areas include: 1) polar coordinate transformations: a means of enhancing the faint outer spiral pattern of M83; 2) ratios of spectral bands in M82 indicate that the H $\alpha$  filaments are not of a reflection nature; 3) extending the Gull maximum entropy algorithm beyond the convergence point produces better restoration with little artifact. Applications to M87; 4) attempts to recover images from the phase of the Fourier transform produce uncertain results in real objects. Applications to M87; 5) a proposed algorithm to statistically identify more unique morphological types of galaxies is illustrated based upon the correlation of images; 6) modeling of complex nebulosity in Lick H $\alpha$  101 with a median filter in order to automatically catalogue stars with a threshold algorithm; 7) relative color and polarization in R-Monocerotis indicate a hollow, cone shaped, dusty reflection nebula; 8) CCD type aliasing. Periodic scenes can be corrupted by aliasing if the image forming optics are of too high a quality; 9) illusions induced by sampling frequency beating. These illusions can be eliminated by doubling the picture size with the Sampling Theorem, and 10) low dynamic range induced illusions. Unexpected structure can appear in an FFT if the dynamic range of the image is small.

## CONTENTS

I. INTRODUCTION -----	1-1
II. POLAR COORDINATE TRANSFORMATIONS--M83 -----	2-1
III. MULTISPECTRAL RATIOS--M82 -----	3-1
IV. EXTENDED MAXIMUM ENTROPY RESTORATION--M87 -----	4-1
V. RESTORATIONS FROM THE PHASE--M87 -----	5-1
VI. PRINCIPAL COMPONENT MORPHOLOGICAL TYPES--A Proposal -----	6-1
VII. AUTOMATED COMPUTATION OF STELLAR MAGNITUDES IN NEBULOSITY--LICK H $\alpha$ 101 -----	7-1
VIII. COLOR AND POLARIZATION IN R-MONOCERCUTIS -----	8-1
IX. CCD ALIASING -----	9-1
X. SAMPLING FREQUENCY BEATING INDUCED ILLUSIONS -----	10-1
XI. LOW DYNAMIC RANGE INDUCED ILLUSIONS -----	11-1
XII. SUMMARY AND CONCLUSIONS -----	12-1
REFERENCES -----	13-1

### Figures

1. M83 contrast enhanced to display the background sky and large-scale emulsion inhomogeneities -----	2-2
2. M83 polar coordinate transformation -----	2-3
3. M83 after retransforming from polar coordinates and after rotational smearing of 30 degrees with a median filter -----	2-4
4. M82 ratio image of H $\alpha$ /103a0 -----	3-2
5. M82 ratio image of H $\alpha$ /103aD -----	3-3
6. M82 ratio image of H $\alpha$ /103aE -----	3-4
7. Restoration of a noiseless blurred target -----	4-2
8. Restoration of a blurred and decimated image -----	4-3
9. M87 mosaic -----	4-4

10.	Test target for restorations from the phase -----	5-3
11.	M87 mosaic of restorations from the phase -----	5-4
12.	Demonstration target illustration of the principal component transformation -----	6-4
13.	Lick Ha 101 stellar catalogue map -----	7-2
14.	R-Monocerotis reflection nebula -----	8-2
15.	R-Monocerotis polarization coded for brightness -----	8-4
16.	R-Monocerotis polarization vector display -----	8-5
17.	Summary of sampling processes -----	9-4
18.	Effects of CCD-style undersampling on a simple sinusoidal spoke target -----	9-6
19.	Sampled sinusoids showing interference effects of the sampling function -----	10-3
20.	Sinusoid target showing interference patterns as hyperbolae at center and in central regions of the four edges -----	10-4
21.	Sinusoidal target showing artifact suppression after twofold size expansion using the similarity theorem (sinc interpolation) -----	10-5
22.	Quantization artifacts in sinusoids -----	11-2

## SECTION I

### INTRODUCTION

Astronomy has traditionally made great use of imagery, but this data has almost exclusively been evaluated via the photographic process. With the advent of the unmanned planetary missions and digital cameras, techniques for processing digital images have been developed and are beginning to be applied in astronomy. The advantages of digital images over photographic ones are very great and, with the development of new algorithms and cameras, become greater all the time. It is thus of importance to search for applications and disseminate digital techniques to the astronomical community at large. When Space Telescope becomes operational, the quantity and unprecedented quality of the calibrated digital images returned will call for every available processing means at our disposal. This report is intended to provide a few of those means.

This work was performed during 1980 at the Image Processing Laboratory (IPL) of JPL under FY80 RTOP #389-41-01. It represents a continuing effort (References 1, 2, and 3) to identify and develop new image processing applications to astronomy. Additional goals of this research are the further education of the astronomical community in digital image processing techniques and the expansion of methods for analysis of high-quality space telescope imagery when it becomes available. Hopefully, others will be inspired to find applications to their own disciplines.

This report is divided into twelve sections. Sections II through XI present techniques applied to a major topic. The data used and the techniques involved are described in detail, along with photographs and plots of the results. Section XII gives conclusions that can be made as a result of this work.

## SECTION II

### POLAR COORDINATE TRANSFORMATIONS - M83

It is often advantageous to transform images geometrically into other than Cartesian coordinate systems. Two reasons are commonly given for this (Reference 4):

1. To take advantage of symmetry in the object.
2. To generalize the effect of an otherwise Cartesian algorithm.

As an illustration of such a process, deep plates of M83 obtained by Dr. Willem Wamsteker of the ESO were selected. Figure 1 illustrates M83 and what appear to be spiral arms in a ring surrounding the object. In order to reveal faint azimuthal surface brightness it would be desirable to smear the object in rotation, improving the signal to noise for low frequency azimuthal structure. Conventional filters are usually coded to operate in a Cartesian system only and would not normally be of use to us in this case. If, however, we were to transform the image to polar coordinates such that each line represented a different radial profile, extending in azimuth from  $0^\circ$  to  $360^\circ$  we would be able to apply a rotational filter by merely operating upon the polar coordinate image. A subsequent inverse transformation would return us to the original geometric representation.

Figure 2 displays the polar coordinate image of M83 performed after a 41 by 41 element median filter (Reference 4) to suppress small stars. The left edge of the picture is the galaxy nucleus, the lines extending from the top down clockwise about the nucleus from the right. Figure 3 illustrates M83 after retransforming to Cartesian coordinates again. In Figure 3, M83 has been rotationally smeared by  $30^\circ$ . This was accomplished by operating a vertical median filter of length  $30/360$  NL on the polar coordinate image, where NL is the number of lines in the image. Several large stars were not eliminated by the filter and have been smeared. A faint outer spiral arm to the upper right of M83 can now be followed considerably further than in the original image.

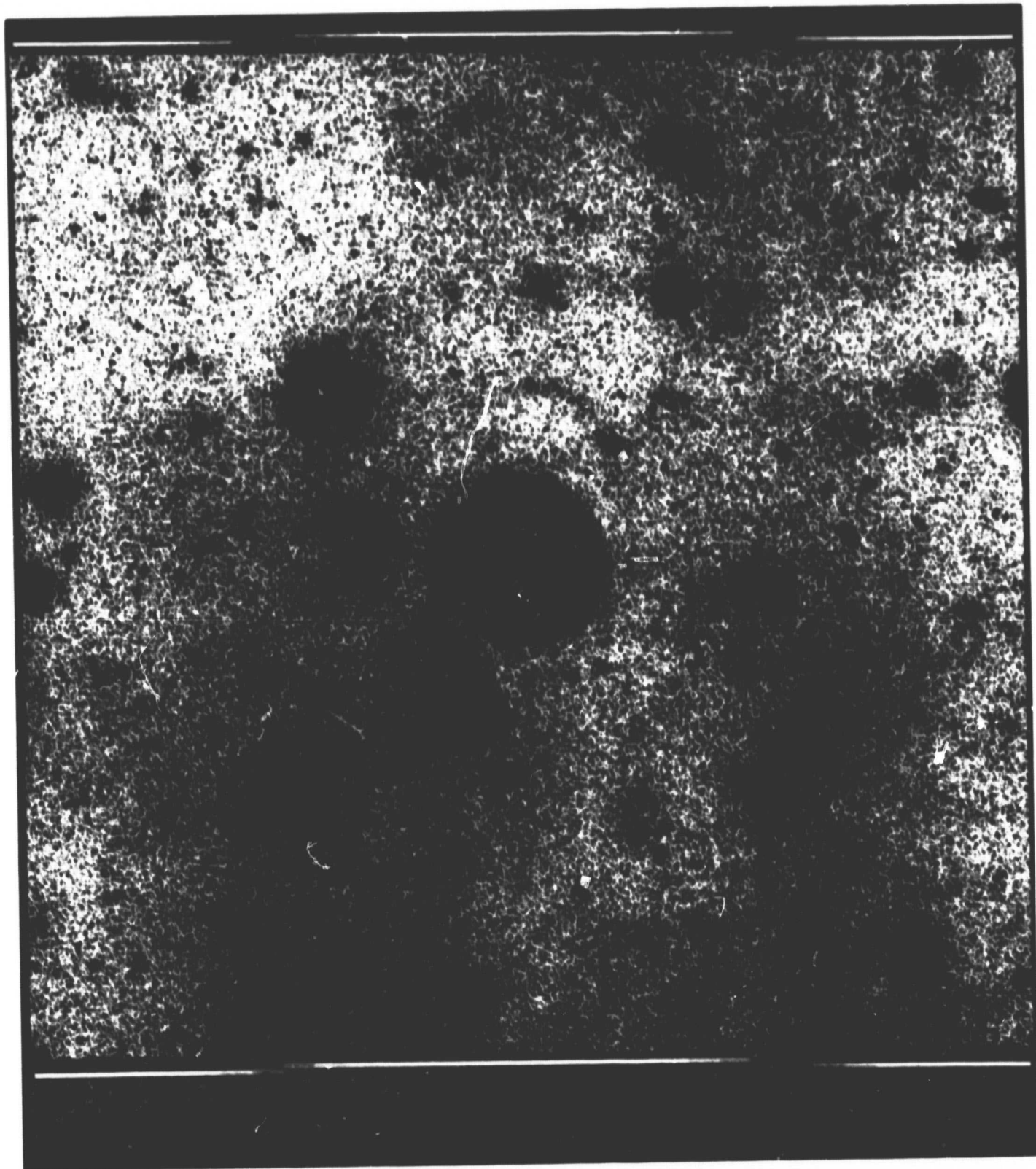


Figure 1. M83 contrast enhanced to display the background sky and large-scale emulsion inhomogeneities. Extended faint azimuthal spiral arms are visible.

ORIGINAL PAGE IS  
OF POOR QUALITY

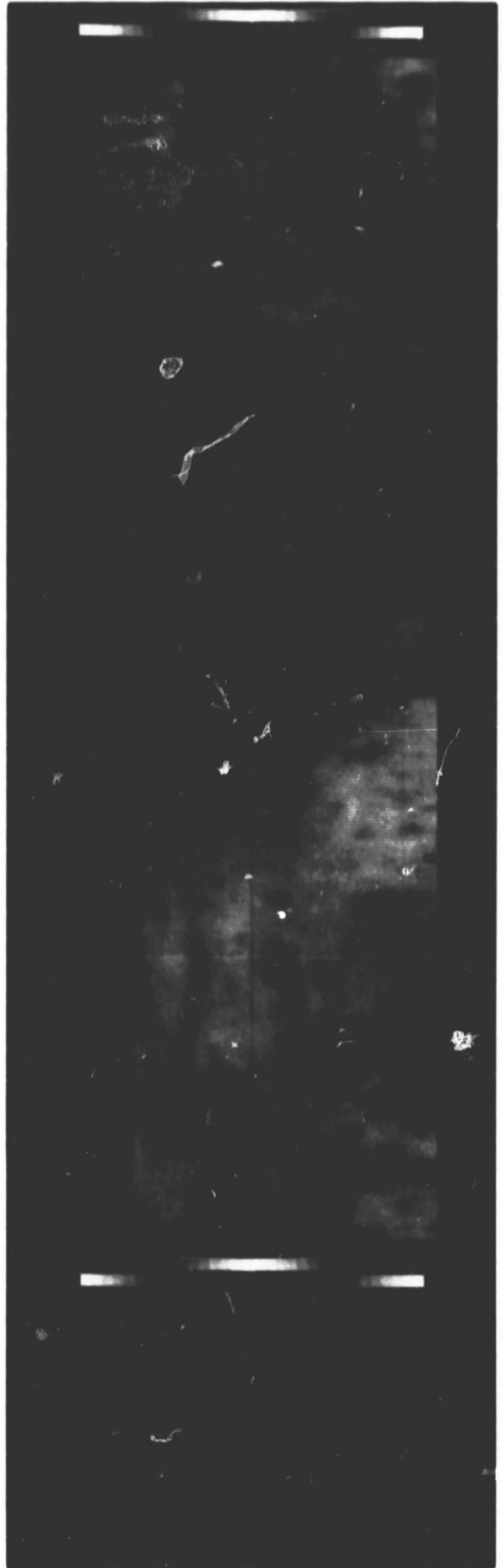


Figure 2. M83 polar coordinate transformation. The lines correspond from top to bottom with radial profiles clockwise about the galaxy nucleus beginning from the right. The nucleus lies along the left edge. A 40 by 40 median filter was applied before the transformation.

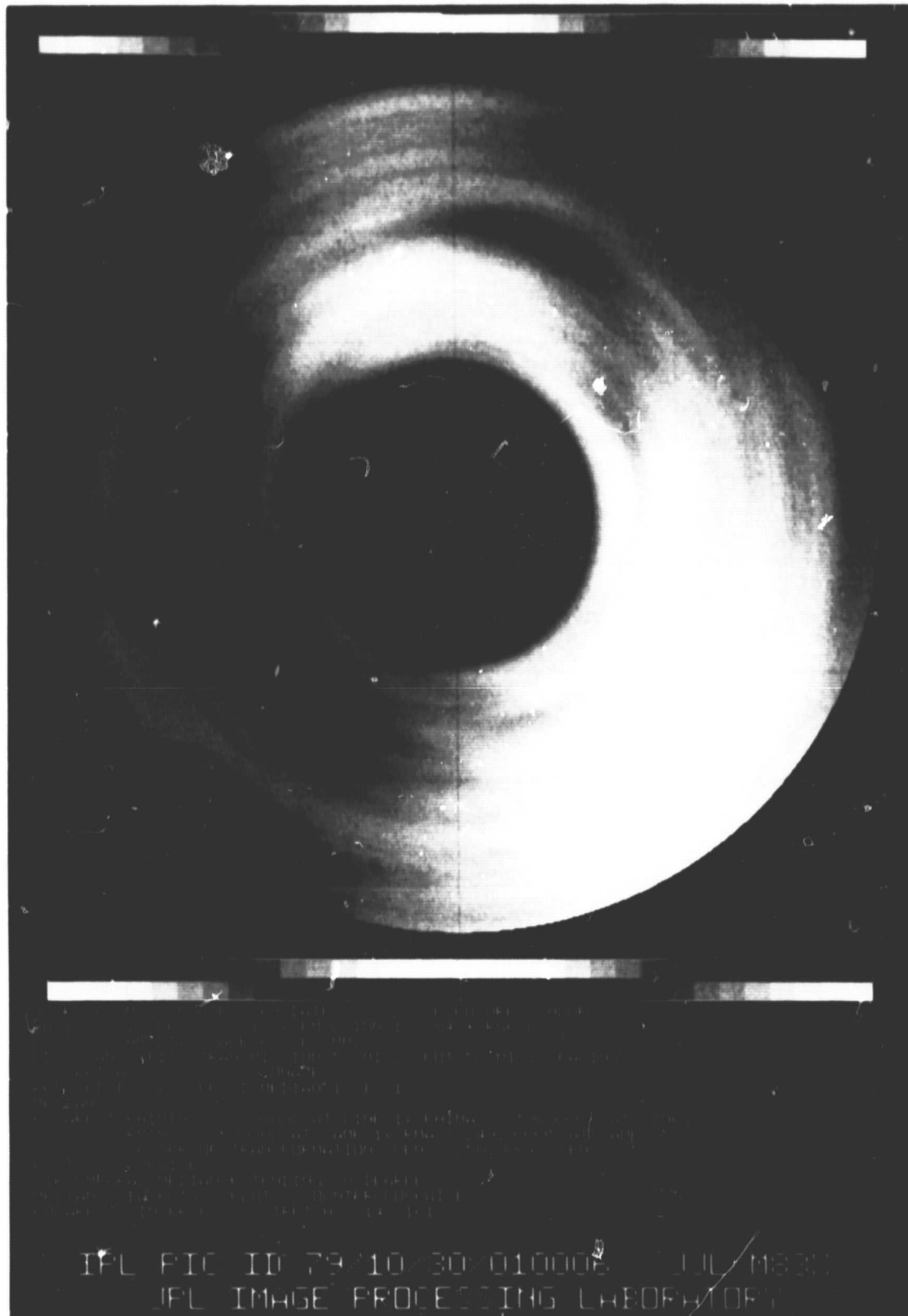


Figure 3. M83 after retransforming from polar coordinates and after rotational smearing of 30 degrees with a median filter to improve the azimuthal signal to noise at low spatial frequencies.

### SECTION III

#### MULTISPECTRAL RATIOS - M82

Plates of M82 obtained by Dr. Alan Sandage and processed previously for color and polarization (Reference 3) have been ratioed to determine the nature of the H $\alpha$  source. The two theories for the H $\alpha$  source are reflection of H $\alpha$  from the nucleus off of the filaments (Reference 5), and emission of H $\alpha$  from the filaments themselves (Reference 6). Figures 4, 5, and 6 illustrate the H $\alpha$ /broad band ratios in the sense H $\alpha$ /103a0 (blue), H $\alpha$ /103aD (green), and H $\alpha$ /103aE (red) respectively. From an inspection of Figures 4-6 it is apparent that the ratio of H $\alpha$ /broad band is a strong function of color, being the most distinct in the blue. This would argue against the source of H being reflection off of dust in the filaments. If the source of all filament irradiance were the nucleus then the filaments should remain constant in all the ratios.

The white regions to upper right and lower left in Figures 4-6 are due to division by small numbers close to the sky background and are not real.



Figure 4. M82 ratio image of H $\alpha$ /103a0.



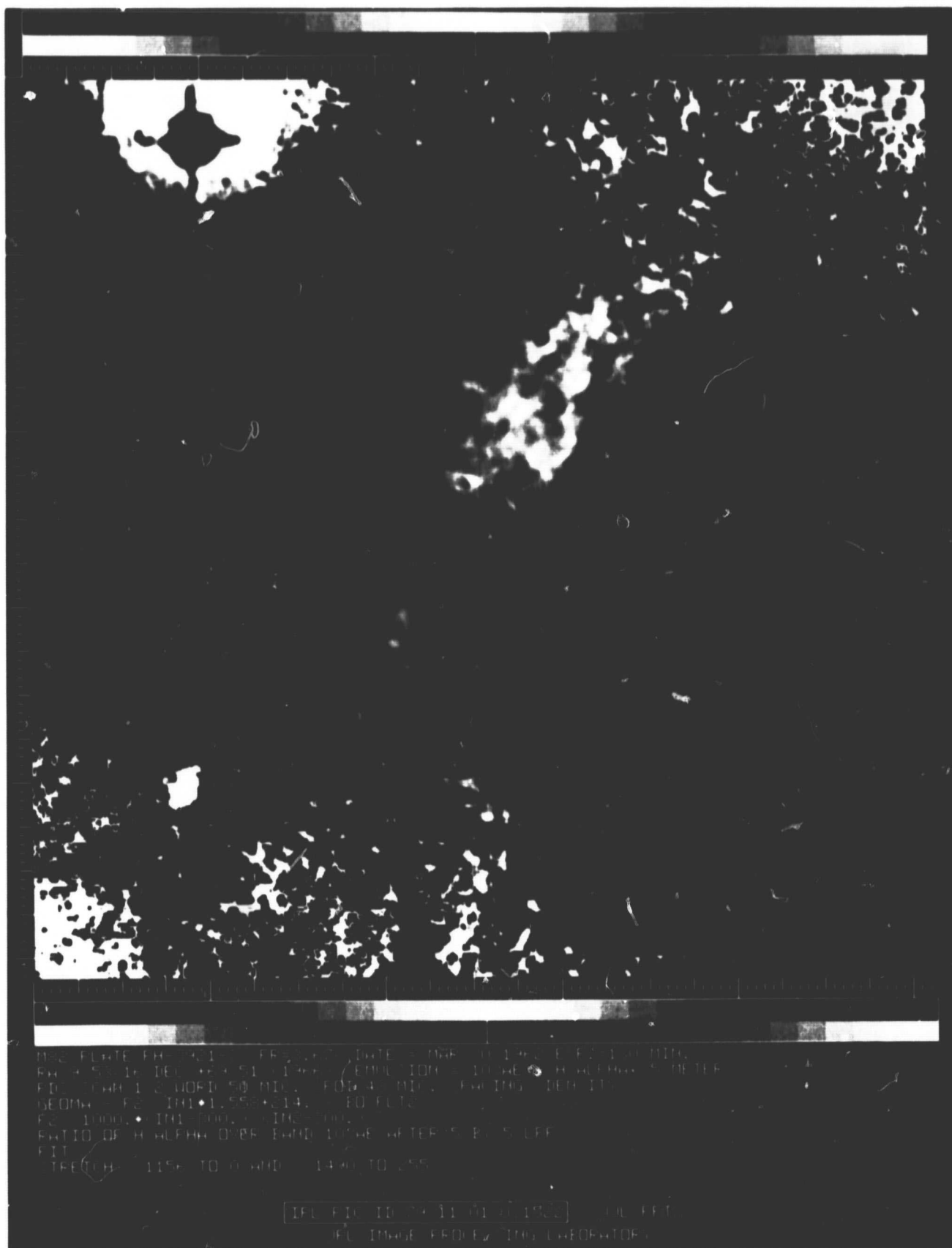


Figure 6. M82 ratio image of  $H\alpha/103aE$ .

## SECTION IV

### EXTENDED MAXIMUM ENTROPY RESTORATION - M87

In Reference 3, results were presented for the maximum entropy restoration algorithm developed by Dr. Stephen Gull (Reference 7). It was shown that the algorithm possessed the valuable quality that it introduced a minimal amount of ringing; however, it also was so conservative as to produce only a slight improvement in resolution. The algorithm has been modified to continue the restoration process beyond the normal convergence point by incrementing the quantity  $\lambda$  by successive multiplication. In Figure 7 a noiseless target (upper left) was blurred by an 11 by 11 element box filter and restored by the extended maximum entropy technique (center left) and, for comparison, by a Wiener filter with a signal to noise of 15 (center right). The restorations are now virtually identical, a considerable improvement over the old algorithm discussed in Reference 3. To the lower left is the chi-squared residuals map with the MTF of the 11 by 11 filter to its right.

In Figure 8 a test target has been blurred (upper right) and then decimated (lower left). The extended maximum entropy algorithm has been able to restore the characters to a legible level by ignoring missing pixels. It would not be possible to operate a linear filter on such an image.

For application to a real object, images of M87 obtained by Drs. Arp and Sulentic were used. In Figure 9 each row contains the M87 original image to the left, the extended maximum entropy restoration made from the image to its left at center, and the chi-squared residuals to the right. The M87 image in the left lower row is the result of subtracting a model of the sky + galaxy halo from it in order to aid the non-negativity constraint. A considerable resolution gain of about 80% is evident, most noticeable in the lower row.

The restored images suffer from little artifact and are superior to linear restorations. This algorithm should be preferred to linear filters when the true nature of the object is unknown.

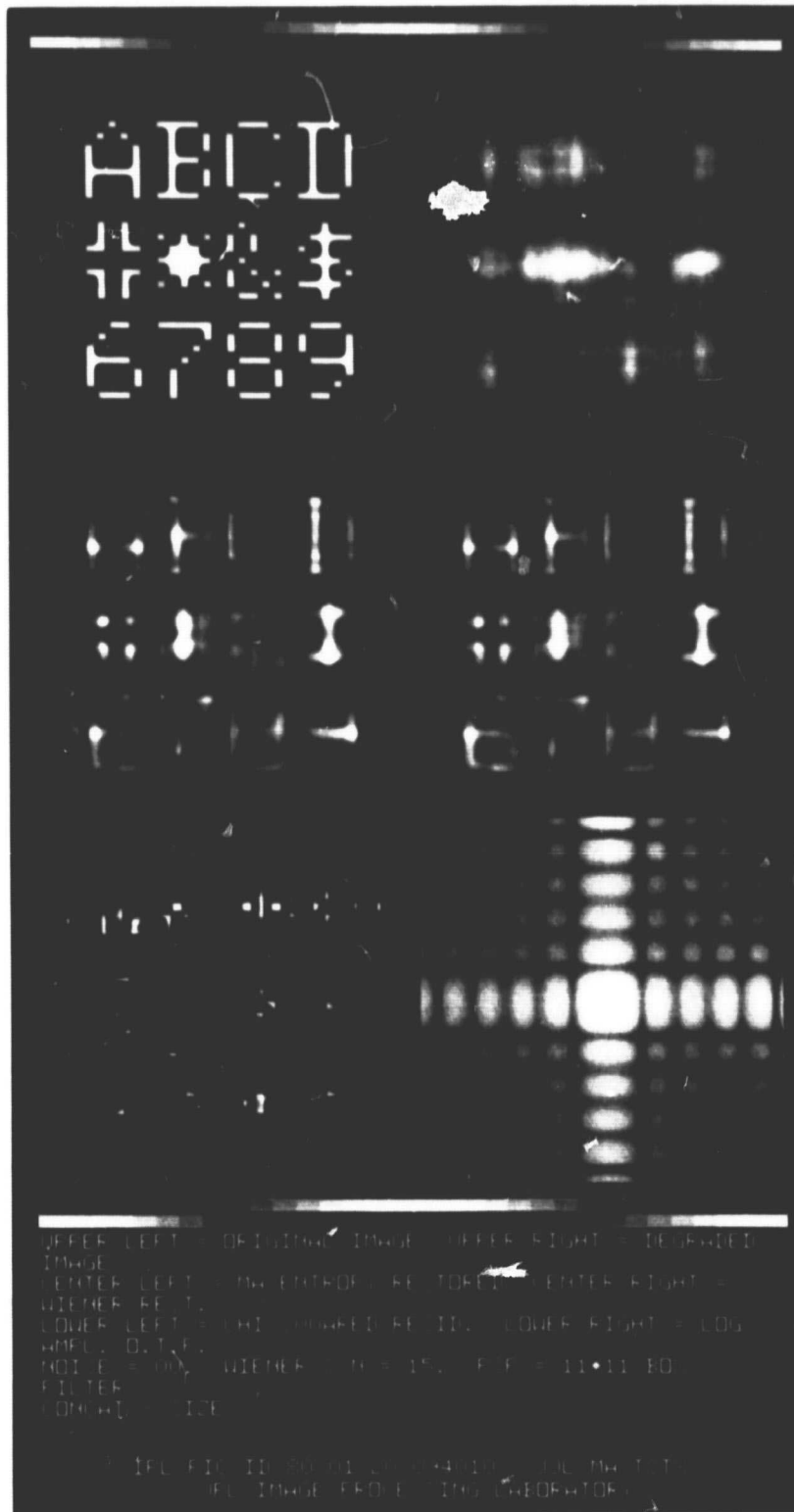


Figure 7. Restoration of a noiseless blurred target; (upper left) original; (upper right) blurred with an 11 by 11 box-filter; (center left) extended maximum entropy; (center right) Wiener; (lower left) maximum entropy chi-squared residuals; (lower right) transfer function (MTF) of the boxfilter. The Wiener signal to noise was 15.

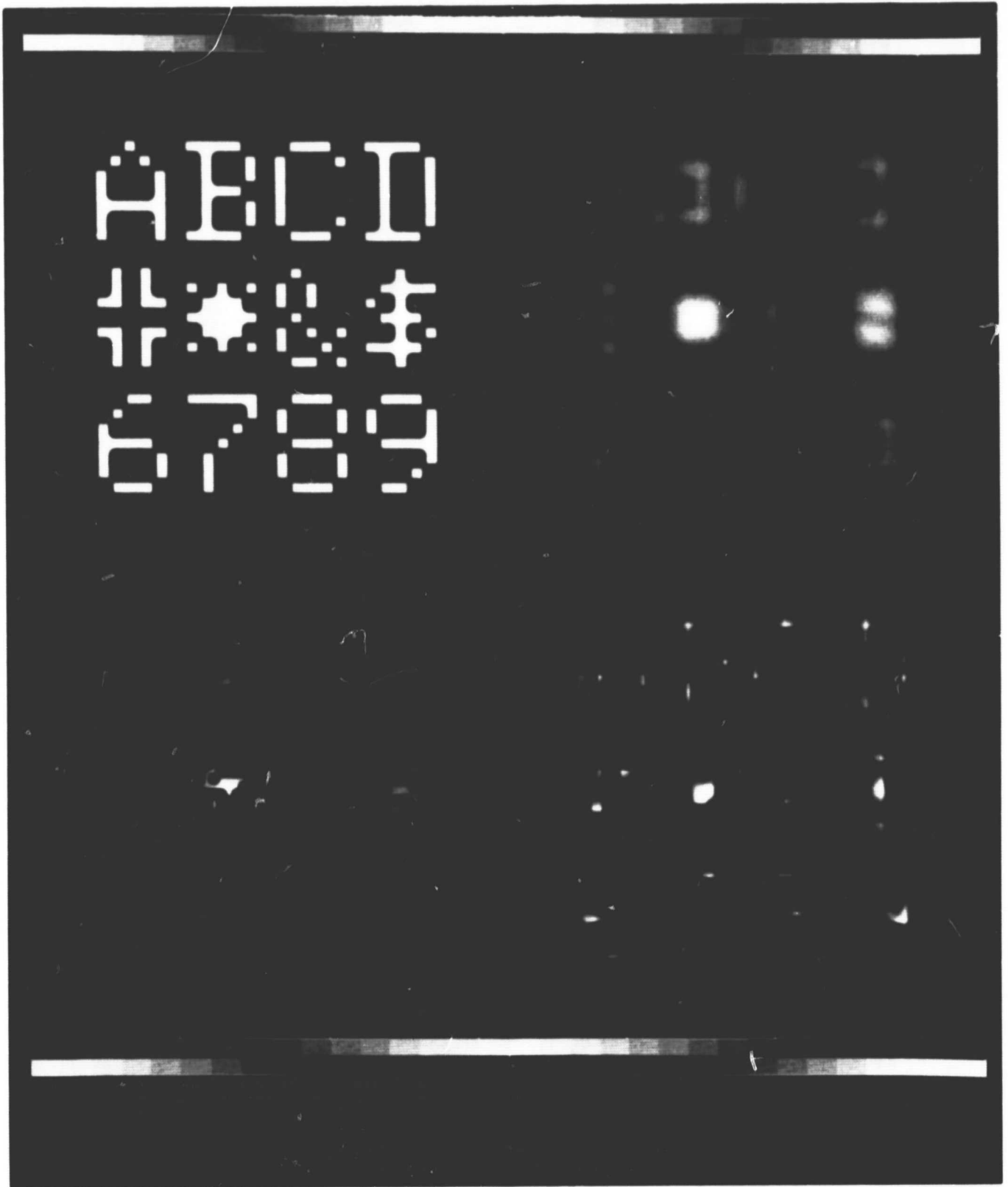


Figure 8. Restoration of a blurred and decimated image; (top left) original; (top right) blurred with a 7 by 7 boxfilter; (lower left) decimated revision of the top right image; (lower right) extended maximum entropy restoration.

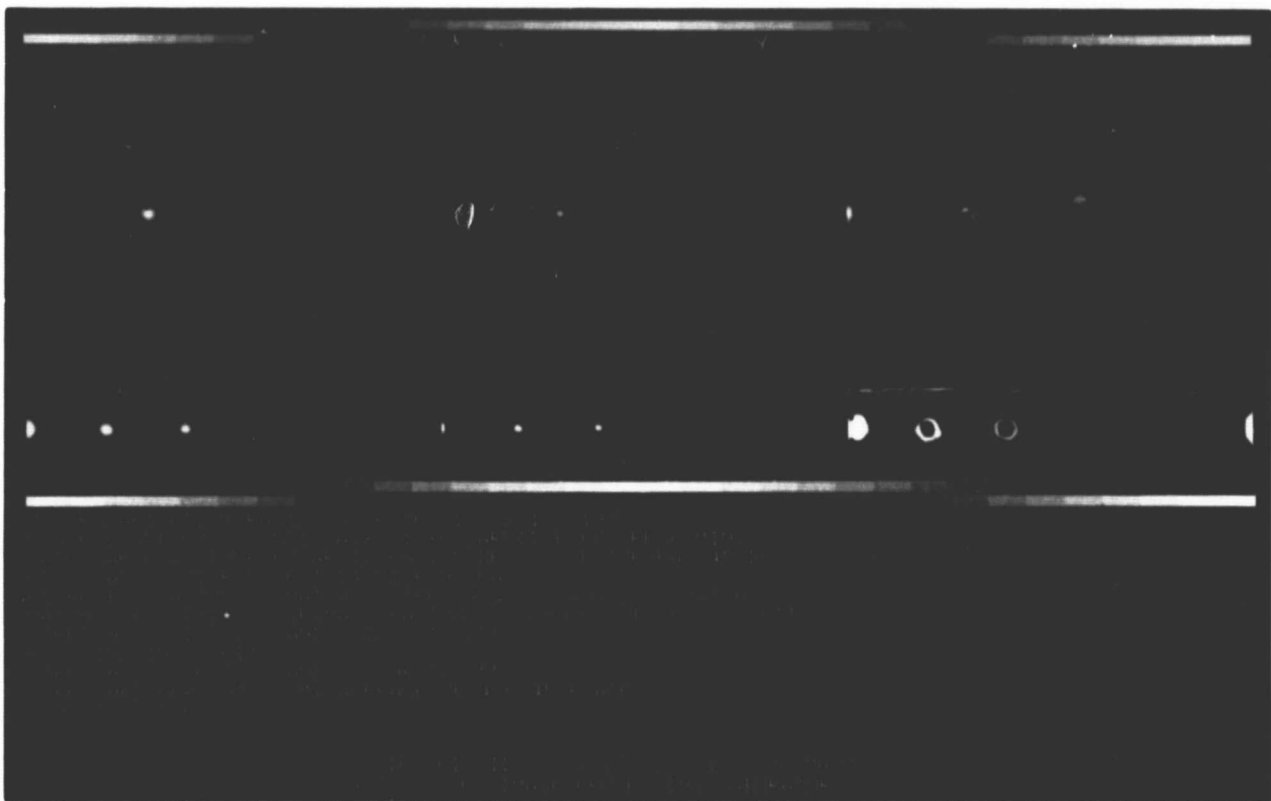
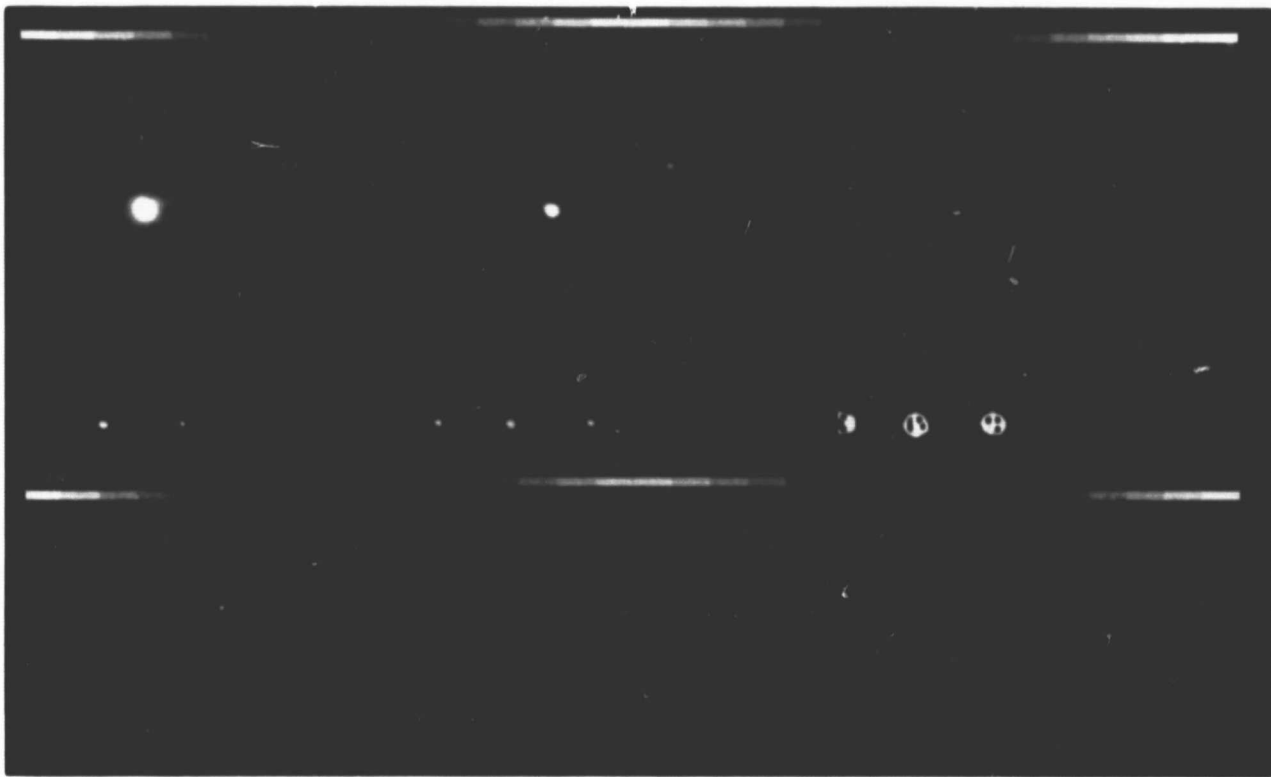
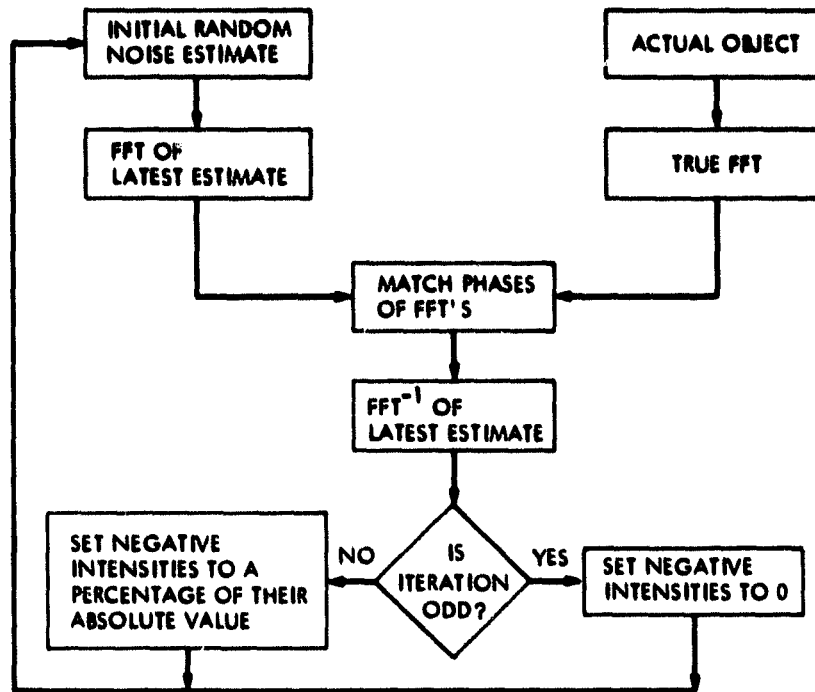


Figure 9. M87 mosaic. Each row displays the original image at the left of the extended maximum entropy image in the center, and the chi-squared residuals to the right. A model of the sky and the M87 halo was subtracted from the original image in the bottom row.

## SECTION V

### RESTORATIONS FROM THE PHASE - M87

It is possible to recover the amplitude from the phase of a Fourier transform and vice versa provided that the inverse transform has certain properties (such as positivity; all of the necessary conditions are not known). A flow chart is shown below which illustrates the basic concept originally suggested by Fienup (Reference 8).



The strategy is beginning with an initial random noise estimate of an object, to force either the amplitude or the phase of the FFT to match the amplitude or the phase of the true FFT (whichever is known). The inverse FFT of the estimate is corrected for negative intensities and the FFT is once again forced to match the reference FFT. The process continues until a satisfactory image is obtained (if that proves possible). The YES/NO test in the last step is used to "shock" the solution away from degenerating into a repetitive static situation.

Figure 10 illustrates this process using a test target (top center) and a typical initial estimate for the target (top left). All of the other squares represent images recovered from only the phase of the FFT of the test target after 10 iterations, each with a different initial random noise estimate. These images are very similar, and retain the point spread function of the original target (note that any symmetrical, non-axis crossing modulation transfer function would have served).

This concept was applied to an image of M87 in Figure 11. The left and right columns contain the original "test" images at the top and the images recovered from the phase of their FFT below them. The left column used the original image and the right column used the original maximum entropy algorithm restoration. It was not expected that the left column would produce an improved image because the phase of the FFT has been corrupted by film grain noise. In the right image however, the phase has been largely restored even though the amplitude has not been resolution corrected, making this a good candidate for this technique. The results show no improvement in the left column and a questionable result in the right column.

The M87 image may have greatly improved in resolution, however, the row of reference stars below has been obliterated, a result which obviates any physical interpretation of the M87 image itself. The likely answer for failure in this case is initial errors in the phase.

A possible corrective avenue of approach might be to "rig" the image with dummy structure convolved with the blurred image point spread function and then each time the inverse FFT is taken, to replace the dummy structure with the actual unconvolved structure in order to guide the restoration process in the correct direction.



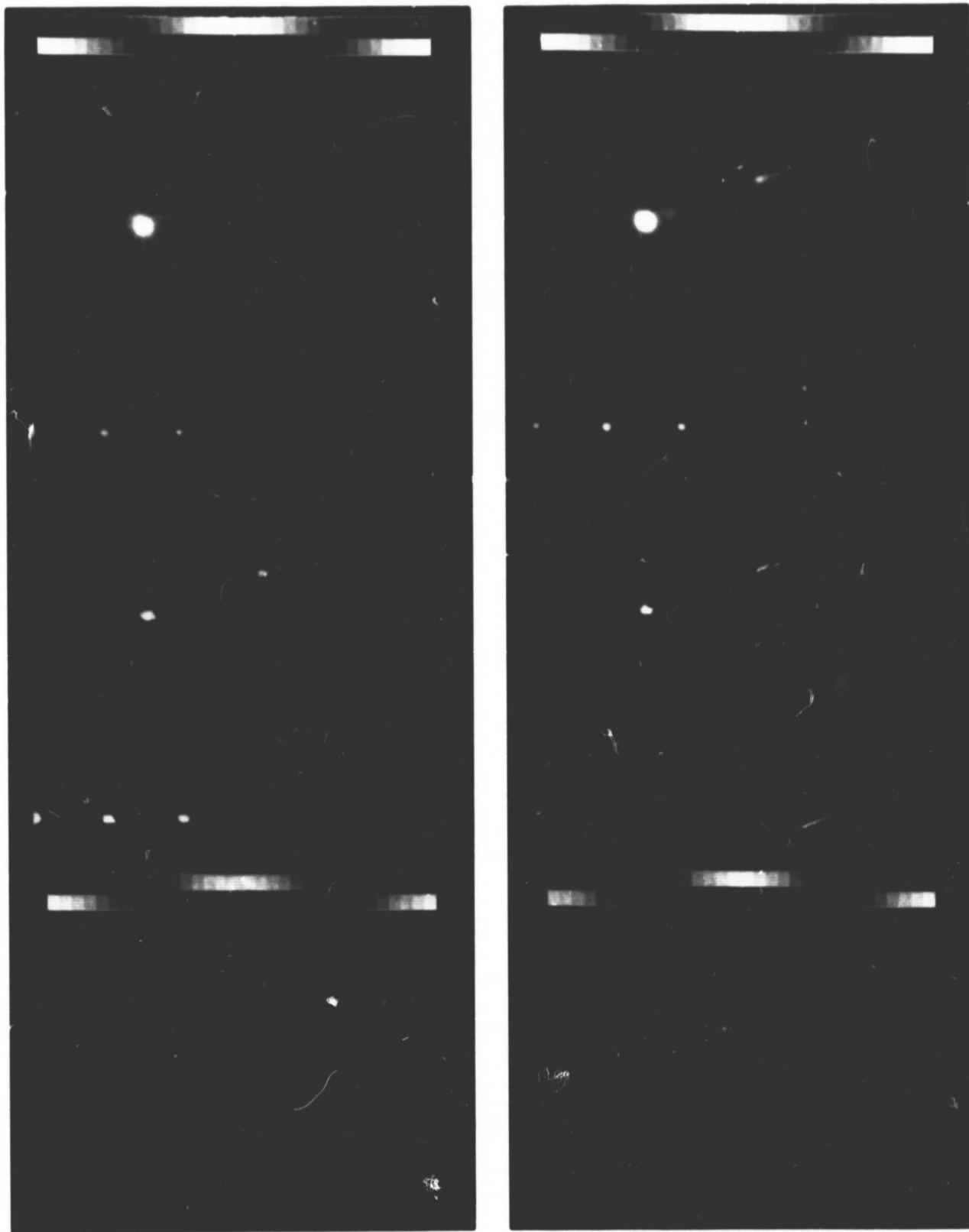


Figure 11. M87 mosaic of restorations from the phase; (top left) original M87 image; (top right) maximum entropy restoration without sky model subtraction; (lower left) restoration from the phase using the upper left image; (lower right) restoration from the phase using the upper right image.

## SECTION VI

### PRINCIPAL COMPONENT MORPHOLOGICAL TYPES - A PROPOSAL

The following formalization was developed after a discussion with Dr. Marius Moles Villamate of Centro Astronomico Hispano-Aleman.

The object of the following topic will be to select from a large selection of galaxies representing all known morphological types the statistically fundamental morphological types, i.e., those which correlate the least with the others and are thus the most unique. In order to accomplish this, we must compute the correlation matrix which consists of the correlation of each galaxy with all of the others.

$$C_{ij} = \frac{1}{\sigma_i \sigma_j} \sum_k (I_{kj} - \bar{I}_j) \cdot (I_{ki} - \bar{I}_i) ; \begin{matrix} 1 < i < N \\ 1 < j < N \end{matrix} \quad (1)$$

where

$I$  = intensity of pixel  $k$  in image  $i$  or  $j$

$\bar{I}$  = mean intensity of image  $i$  or  $j$

$N$  = total number of images

$\sigma$  = standard deviation of image  $i$  or  $j$

$C_{ij}$  is an  $N$  by  $N$  matrix

The eigenvalues of  $C_{ij}$  must be computed next.

Once the eigenvalues have been computed the eigenvectors can be computed from:

$$R^t C R = C' \quad (2)$$

where

$t$  = transpose

$R$  = eigenvector matrix

$C'$  = matrix whose diagonal is the eigenvalues

The principal component transformation (References 3 and 9) of conventional images into uncorrelated images is given by multiplying matrix R with the conventional images:

$$\begin{pmatrix} I'_1 \\ I'_j \\ \vdots \\ I'_N \end{pmatrix} = R \begin{pmatrix} I_1 \\ I_j \\ \vdots \\ I_N \end{pmatrix} \quad (3)$$

The eigenvalues represent the information content (variance) of the uncorrelated images  $I'$ .

Thus, if there are  $l$  large eigenvalues and  $n-l$  smaller ones it means that only  $l$  unique images exist in the original set of  $N$  images  $I$ , and that the other  $n-l$  images are merely linear combinations of the former  $l$  images. This tells us how many unique morphological types exist but it does not specify which ones. Notice that for arbitrary pictures the unique images may prove to be linear combination of the image provided; however, we know from the physical positivity constrain on intensities that virtually no linear combinations are possible which provide only positive images. This means that the set of unique morphological types must be single images contained in the set provided.

The unique images can be identified from the top row of the R matrix which is that vector of weights which, when multiplied by the input set of galaxies, provides that image with the largest eigenvalue. The principal component image with the largest eigenvalue is the optimal average of the input images, and consists of the weighted rows of the input images. The weighting is large if an image is "typical", i.e., is highly correlated with its neighbors, and is small if it is different, i.e., is unique among the set of input images (a distinct morphological type).

Figure 12 illustrates the process described thus far. The top row consists of four images, only two of which are unique. The third image from the left is the average of images 1 and 2 and the fourth image consists of 20% of image 1 plus 80% of image 2. The correlation matrix  $C_{ij}$  is:

$$C_{ij} = \begin{pmatrix} 1.0 & 0.46 & 0.85 & 0.62 \\ 0.46 & 1.0 & 0.85 & 0.98 \\ 0.85 & 0.85 & 1.0 & 0.94 \\ 0.62 & 0.98 & 0.94 & 1.0 \end{pmatrix}$$

From C the eigenvalues can be computed as:

3.381  
0.620  
0.001  
0.001

only the top two of which are significant, indicating that only two unique images exist.

The eigenvector matrix R can be computed as:

$$R = \begin{pmatrix} 0.4282 & 0.4948 & 0.5401 & 0.5293 \\ -0.7831 & 0.5277 & -0.1494 & 0.2929 \\ 0.2687 & -0.1563 & -0.6998 & 0.6431 \\ -0.3619 & -0.6724 & 0.4428 & 0.4696 \end{pmatrix}$$

Each of the four images (the principal component images) on the bottom row of Figure 12 are obtained from the R matrix:

$$\begin{pmatrix} \#1 \\ \#2 \\ \#2 \\ \#4 \end{pmatrix}_{\text{bottom}} = R \begin{pmatrix} \#1 \\ \#2 \\ \#3 \\ \#4 \end{pmatrix}_{\text{top}}$$

From an inspection of the top row of the R matrix it can be seen that the left two values are the smallest, indicating that the left two images in the top row are the most unique of the set of 4 images we began with.

From a selection of a hundred images of all morphological types each face-on, intensity rotation and size normalized it should be possible either to select a few parent types or at least to rank the images in importance.

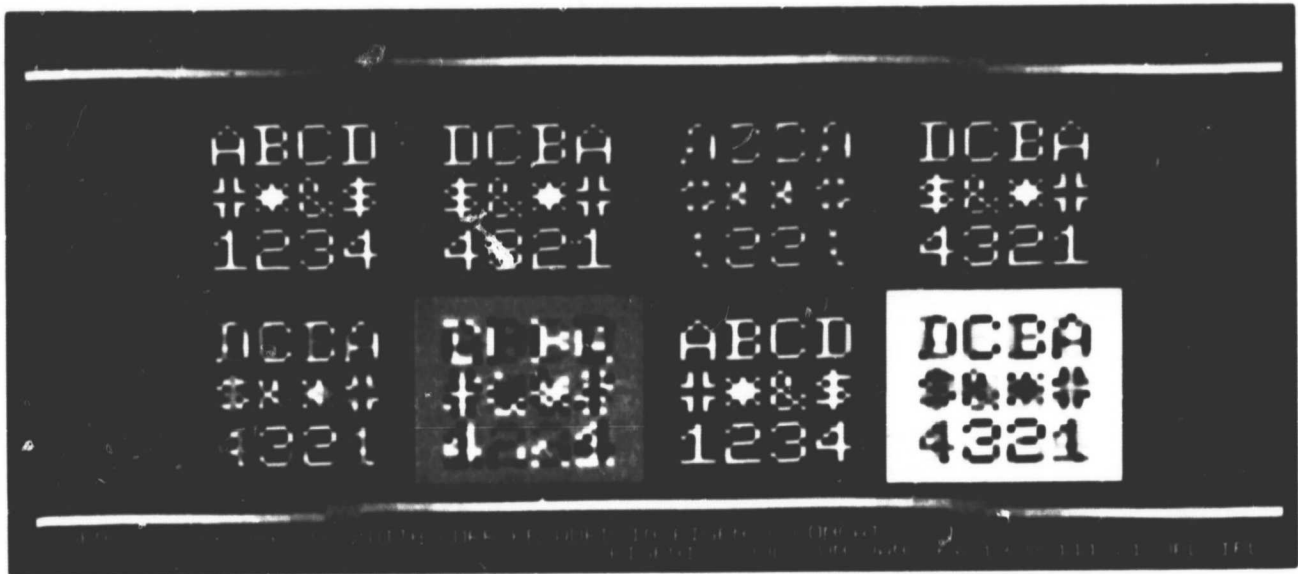


Figure 12. Demonstration target illustration of the principal component transformation. The upper four images are linear combinations of two images. The lower four images are normalized principal component images of the upper four images ranked from left to right in decreasing eigenvalue. From the lower images we can determine which of the upper four are the original two images.

## SECTION VII

### AUTOMATED COMPUTATION OF STELLAR MAGNITUDES IN NEBULOSITY - LICK H $\alpha$ 101

One of the problems encountered in automated methods of determining stellar magnitudes is when spatial nebulosity causes the background of the plate to vary. This situation is a serious drawback for stellar cataloging software which relies upon a simple above-threshold criterion for object detection. The median filter offers an expedient if not a very accurate solution to this problem by providing a means of modelling the background without the stars. Once the background is determined it can be subtracted from the image, leaving the stars on a low amplitude intermediate spatial frequency background.

Figure 13 illustrates one of a set of multispectral images of Lick H $\alpha$  101 after the background has been subtracted and the stars catalogued. Considerable confusion exists near the complicated portions of the nebula resulting in numerous false "stars" entered into the catalogue. From the numerical designations it is however quite easy to identify reasonable objects and to select their intensities from among the sorted catalogue entries.

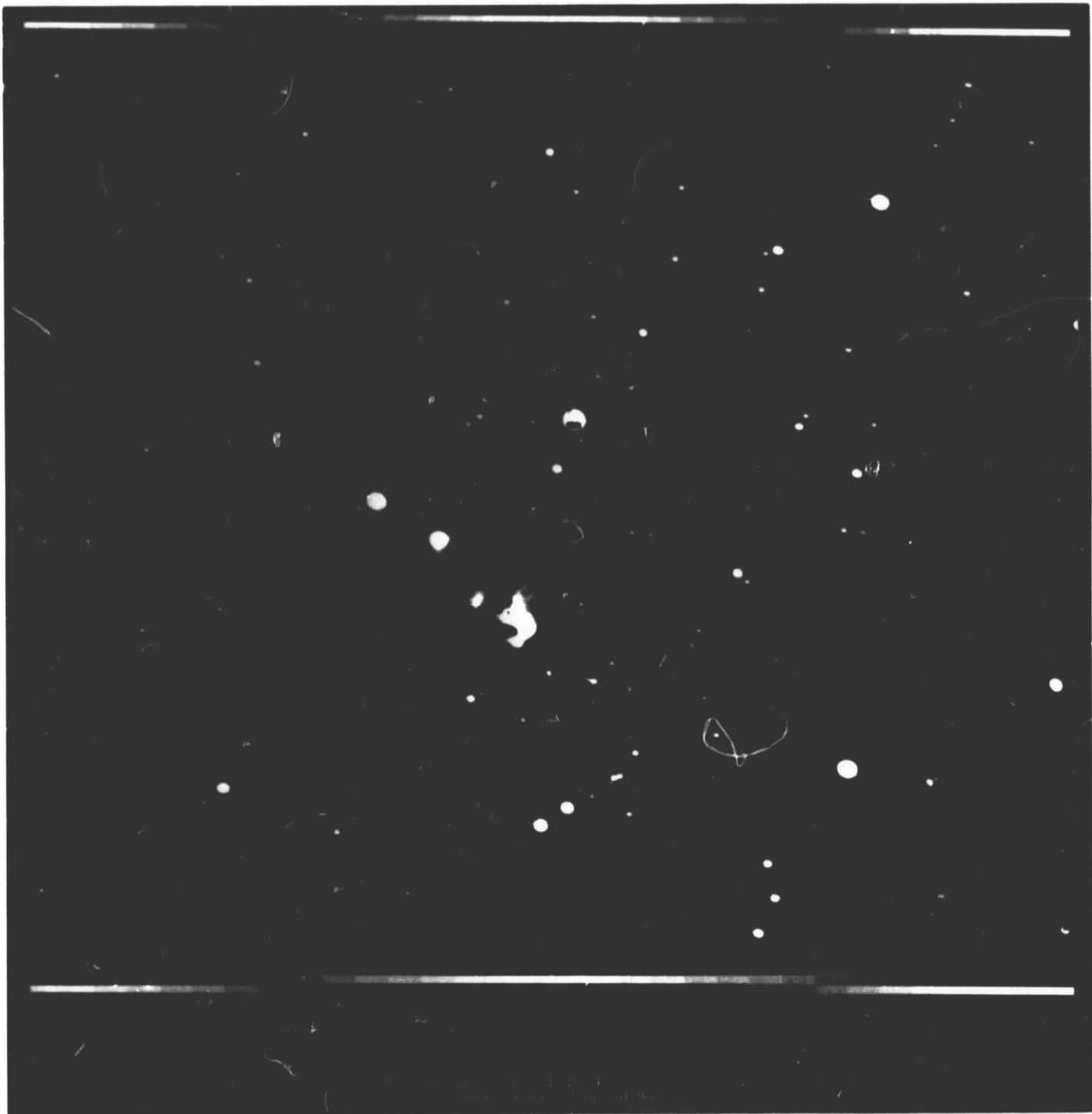


Figure 13. Lick H $\alpha$  101 stellar catalogue map. Stellar images were located by simple threshold search after subtraction of a model of the Lick H $\alpha$  101 reflection nebula. The nebula was modelled with a median filter.

## SECTION VIII

### COLOR AND POLARIZATION IN R-MONOCEROTIS

The enhancement of color and the generation of polarization maps is not new and has been discussed in References 1 and 3. This section is included because, for R-Monocerotis, both are available together and the combination provides an interesting data base on an early type object. Figure 14 is a relative color display produced by normalizing the blue, green, and red plates (103a0, 103aD, 098) and exaggerating the color with a saturation image contrast enhancement in the HSI space (Reference 4). Figures 15 and 16 illustrate polarization (4 percent and above has been saturated to white) and polarization vector orientation respectively. From the vector map it would appear that the large R-Monocerotis nebula is a dusty reflection nebula illuminated by the bright star at its apex. The relative color display shows that the outer reflection nebula is redder than at its center, probably because the light is more highly reddened by scattering at the periphery of the nebula. This would be the case if the nebula were a hollow cone. Light scattered at the sides of the cone would have to travel through more material before exiting toward the observer than would light at the front and back sides. The cone hypothesis is further strengthened because the polarization map is correlated with color, being more highly polarized where the nebula is redder.

Similar maps of the T-Tauri reflection nebula show no color variations whatsoever. The different spectral bands are multiplicative replicas of each other.

Figure 14. R-Monocerotis reflection nebula. The three-color bands were normalized to the same amplitude to reveal differential color. The true color is entirely red.





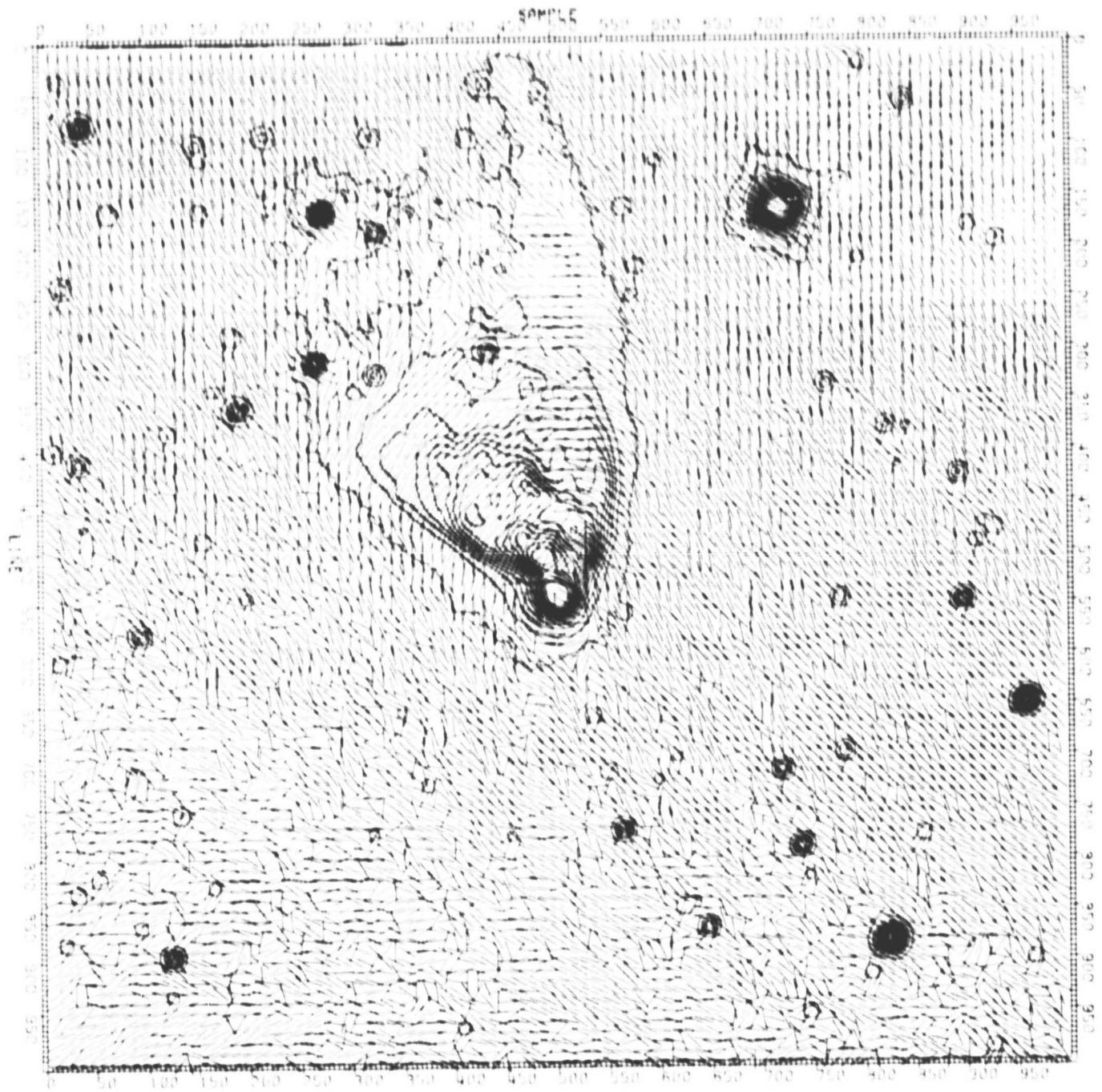


Figure 16. R-Monocerotis polarization vector display.

## SECTION IX

### CCD ALIASING

The following three sections were developed jointly with Dr. Alan Gillespie of JPL and appear in more complete form as Reference 10.

The sampling theorem (References 11 and 12) states that a band-limited function whose Fourier transform is zero at frequencies greater than some frequency  $S_c$  is fully specified by values spaced at equal intervals not exceeding  $(2 S_c)^{-1}$ , with the exception of harmonic terms with zeroes at the sampling points. Real scenes have extended spectra, but may be band-limited by filtering in the atmosphere, the optics, or the sensor itself. CCD's and other solid-state sensors cannot band-limit a signal properly because the sample dimension is at most equal to the sample spacing. Thus when the point-spread function (PSF) of the combined atmosphere and optics is similar in size to individual receptors of the CCD, care must be taken in interpreting resulting images.

The process of sampling is briefly summarized in Figure 17. A continuous scene might have an extensive spectrum  $F(s)$  as shown in Figure 17a. A CCD or other solid-state camera with a square receptor (pixel) of width  $d$  will have a transfer function specified by  $\sin(\pi ds)/\pi ds$ , or  $\text{sinc}(ds)$ , where  $s$  is the spatial frequency. The energy spectrum available to the CCD for measurement is  $F(s) \cdot \text{sinc}(ds)$ , a sinc function with attenuated side lobes shown in Figure 17b. When the scene is sampled at an interval  $p$ , the continuous spectrum is converted to a repetitive and overlapping array of discrete spectra with a periodicity of  $p^{-1}$  in the frequency domain. For CCD cameras,  $d \leq p$  and the fundamental spectrum is significantly contaminated by energy from adjacent spectra (Figure 17c). For example, at 0.25 cycles/pixel, half the energy may be aliased. If  $d > 2p$ , the only contamination would be from side lobes of neighboring spectra. Figure 17d illustrates such a spectrum, specified by:

$$I(s) = \sum_{n=-\infty}^{\infty} F\left(s + \frac{n}{p}\right) \cdot \text{sinc}\left[d\left(s + \frac{n}{p}\right)\right] \quad (4)$$

Even so, as evaluation of the above series shows, roughly one quarter (the exact amount depends on  $F(s)$ ) of the energy at 0.25 cycles/pixel is aliased.

In an image, aliased energy is manifest as fine detail which is distorted in two ways: small features may appear too large and their locations may be shifted by up to  $d/\sqrt{2}$ . As Root (Reference 13) has illustrated, for most scenes the distortions caused by CCD - style undersampling are not severe and indeed may improve the appearance of the image by increasing the "sharpness" and the amount of detail visible. This is because of the large amount of energy aliased when  $d = p$ . Most such images can be interpreted correctly, provided the scene is familiar to the analyst. Simple geometric

targets may be grossly distorted, however, and scenes containing repetitive geologic structure or periodic atmospheric cloud features may likewise be misrepresented. It should be emphasized that low-pass filtering can do little to reduce these artifacts if any scene detail is to be preserved at all, because fundamental and aliased energy cannot be separated and are both reduced alike. Conversely, high-pass filtering emphasizes the most strongly aliased part of the spectrum, exacerbating interpretative difficulties.

Figure 18 illustrates the visual impact of CCD-type undersampling on a highly structured target. The original "scene" is at the upper left. The picture at the upper right represents the scene band-limited such that sampling at the CCD pixel spacing  $p$  produces isolated periodic image spectra, as in Figure 17d. For comparison, at center left is the image resulting from sampling the original "scene" with  $d = p$  simulating the image from a CCD camera. At bottom are the log amplitude of the Fourier transforms of the top images. Finally, at right center is the CCD image after post-sampling low-pass filtering, illustrating the infeasibility of this approach as a remedy for undersampling.

The essential point is that in the presence of quasi-periodic structure, image information can be so fundamentally altered by CCD-type undersampling and aliasing as to preclude correct visual interpretation. In the properly sampled image (upper right) information in the overlapped spectral region is removed, protecting the analyst from false interpretations by rendering none possible. Further examples of sampling artifacts with various  $d$  and  $p$  may be found in Reference 13.

Once a scene has been undersampled there is no simple procedure for resampling or filtering the data to produce a non-aliased image. This is because phase information has been irrevocably lost during integration for each pixel. Thus such intuitively simple and appealing suggestions as addition of neighboring pixels to simulate original sampling with  $d = 2p$  will fail, at least in detail. Addition of adjacent pixels is a convolution operation specified in one dimension by the kernel  $(0 \ 1 \ 1)$ , which has the Fourier transform

$$G(s) = e^{-i\pi s} \cos \pi s \quad (5)$$

when  $d = p = 1$ . Applied to the image spectrum, this filter modifies the spectrum amplitude by  $\cos \pi s$  and also shifts the phase by  $e^{-i\pi s}$ , yielding a filtered image spectrum of

$$e^{-i\pi s} \cos \pi s \sum_{n=-\infty}^{\infty} F(s+n) \operatorname{sinc}(s+n) \quad (6)$$

which is not at all the same as the intended spectrum specified by

$$\sum_{n=-\infty}^{\infty} F(s+n) \operatorname{sinc} [2(s+n)] \quad (7)$$

This basically reflects the impossibility of separately filtering the individual terms of the series once summation has occurred during sampling.

Aliasing in CCD images is most readily solved by degrading the quality of the image-forming optics. This has the effect of reducing the amplitude of  $F(s)$  at high frequencies so that overlap of the spectra of the sampled scene is negligible. This requires, however, that the optical PSF be approximately gaussian in order to avoid introduction of optical artifacts. Simple defocussing is not a solution because of the onset of spurious resolution in the center of the modulation transfer function at defocusings greater than about  $5.6\lambda f^2$ , where  $\lambda$  is the wavelength of light and  $f$  is the optics  $f$  number (Reference 14). For example, an optical system operating at  $f/15$  and  $5000 \text{ \AA}$  would begin to suffer phase reversals of  $\pi$  at a defocus greater than  $0.6 \text{ mm}$ .

Figure 17. Summary of sampling processes: (a)  $F(s)$  represents the continuous Fourier Transform of a scene projected onto the image plane containing the sensor. Frequency is given by  $s$ . In this instance, the "lens" was assigned an impulse PSF; real optics might have a sinc or gaussian PSF, resulting in decreased amplitude of  $F(s)$  at large  $s$ ; (b) Integration of the image photo receptors of width  $d$  modifies the image spectrum; (c) After sampling the image at intervals of  $p$  the discrete image spectrum is the sum of replicates of the continuous spectrum repeated at frequency intervals of  $p^{-1}$  cycles/pixel. For CCD cameras,  $d < p$  and severe overlapping will occur; (d) If  $D = 2p$  or if the continuous image spectrum is band-limited, overlaps of spectrum replicates can be minimized.

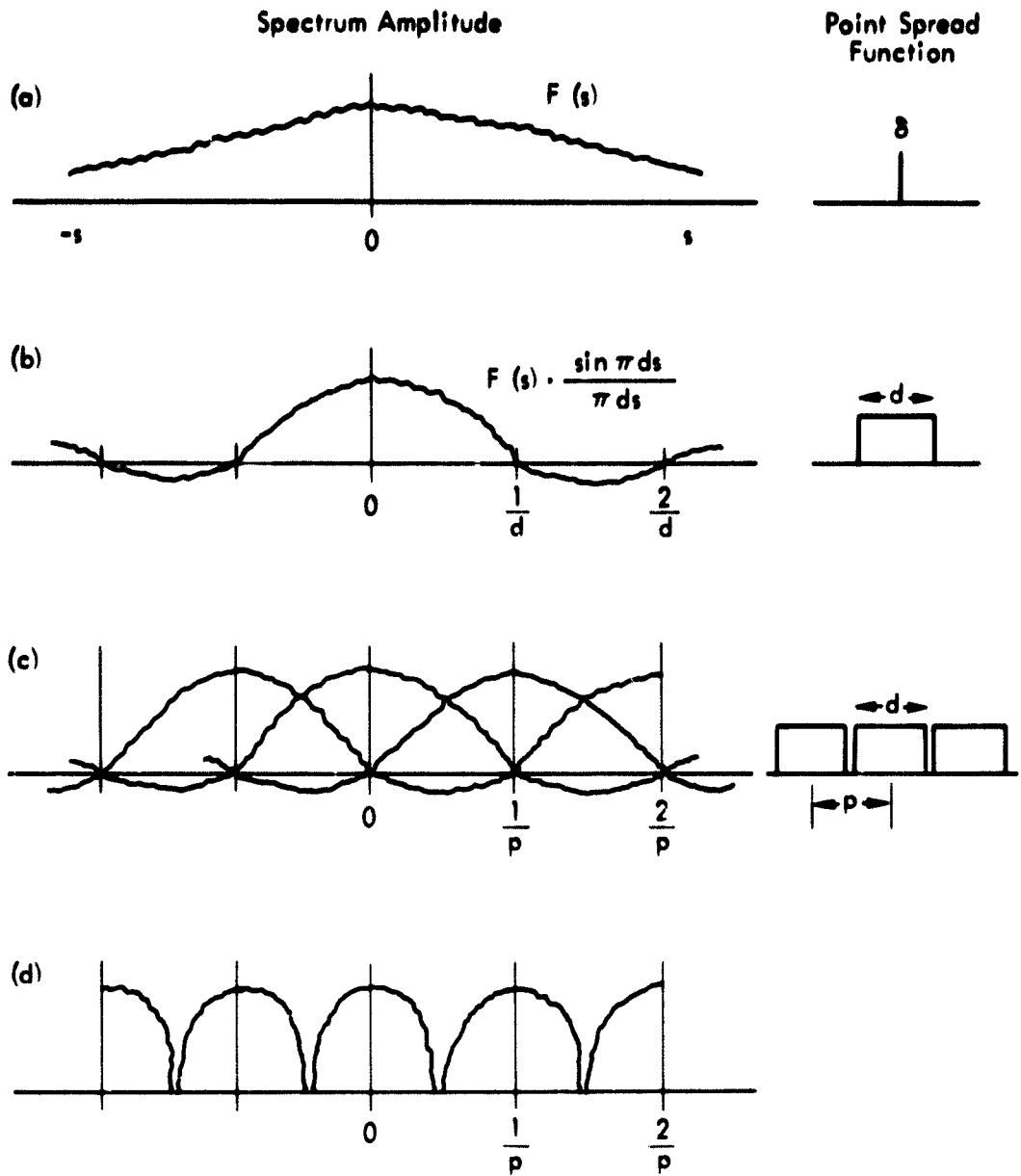
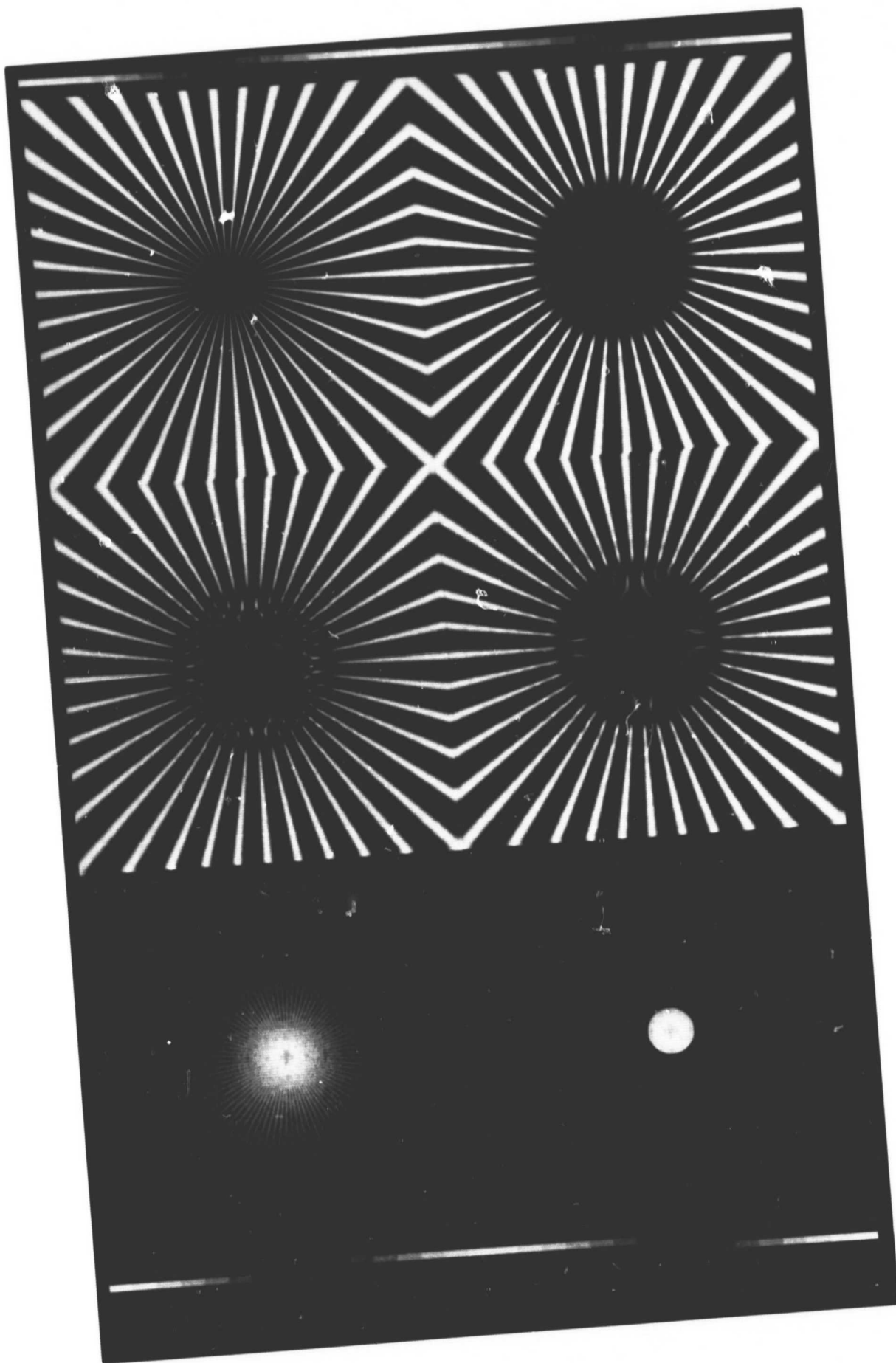


Figure 18. Effects of CCD-style undersampling on a simple sinusoidal spoke target. Upper right: properly sampled image ( $d = 2p$ ) of the band-limited target showing absence of information and artifacts at high frequencies. Center left: target sampled as seen by CCD ( $d = p$ ). Artifacts caused by aliasing are seen instead of high-frequency data. Center right: CCD-sampled image after band-pass filtering showing impossibility of artifact removal. Lower left: spectrum of target; lower right: spectrum of correctly sampled image.



9-7

ORIGINAL PAGE IS  
OF POOR QUALITY

## SECTION X

### SAMPLING FREQUENCY BEATING INDUCED ILLUSIONS

Even if a scene is band-limited and properly sampled, there is no guarantee that it will be recognized from visual inspection of an arbitrary pictorial representation of the digital data. The sampling theorem only states that exact reconstruction of the function is possible. In order to do this correctly, it is necessary to interpolate using the infinite sinc function. This is not easy to do, and usually sampled data is displayed without any effort to reconstruct the original function.

One consequence of failure to reconstruct the continuous image before display is the visible presence, obvious in ordered images, of interference patterns resulting from sampling harmonic constituents of the scene near their nodes, where the amplitude is zero. The frequencies of these nodal zones can be specified in one dimension by observing that the sampling function is given by

$$\sum \delta(x + n) = |\cos \pi x|^\infty \quad (8)$$

Harmonic constituents of the spectrum are waves in space described by a  $\cos 2\pi(\omega x + \phi)$ , where  $A$  is amplitude,  $\omega$  is frequency,  $x$  is spatial position, and  $\phi$  is phase. At some  $x_0$  the wave will be sampled at its crest. If  $x_0$  is taken as the origin, the phase at which sampling occurs is seen to be the periodic function

$$\phi(x) = x(0.5 - \omega) \quad (9)$$

To the eye, the characteristic frequency of  $\phi(x)$  in an image is set by the repetition of the nodal zones, where  $\phi = \pm \pi/2$ . These occur twice per wavelength, so the apparent frequency of the nodal patterns is  $1-2\omega$ . For  $\omega < 0.25$  this nodal frequency exceeds the Nyquist (0.5) and is aliased.

Figure 19 illustrates five waves of different  $\omega$ . Each is oversampled and should resemble a simple sinusoid. Wavelengths from top to bottom are 40, 40/6, 40/10, 40/15, and 40/19 samples. A wave of the sampling frequency has a period of 40/20 samples and is represented as a binary sequence whose amplitude may range from  $\pm 1$  to  $\pm 0$  as a function of phase. It is evident that the simple nature of the sinusoid is masked for wavelengths shorter than about four samples, and that interference patterns may actually be the prominent feature of the image.

Visual inspection of images dominated by waves of frequencies greater than 0.25 cycles/pixel will result in inaccurate interpretation, even though the sampling theorem was observed. Because a discrete frequency spectrum of each of these sampled waves is simply  $\Pi(s) = \delta(s + \omega) + \delta(s - \omega)$ ,

where  $\delta$  is the impulse function,  $s$  is frequency, and  $\omega$  is the frequency of the wave, it follows that the nodal or interference patterns are completely illusory. In fact, they result from incorrect display of the discrete image.

The proper way to reconstruct the continuous image requires convolving the image by sinc  $x$  and resampling at infinitesimally small intervals  $p$ . Clearly this cannot be done, but correct resampling to increase the pixel density in the output picture may be done by inserting the fundamental discrete spectrum into a field of zeroes and by capitalizing on a consequence of the similarity theorem to expand the image. This theorem states that a function  $g(x,y)$  and its transform  $G(f_x,f_y)$  are related by the expression:

$$F [g(ax,by)] = \frac{1}{|ab|} G \left( \frac{f_x}{a}, \frac{f_y}{b} \right) \quad (10)$$

which says that reducing the dimensions of the transform will increase the dimensions of the image in the function domain. This is equivalent to increasing the spacing  $p^{-1}$  between replicates of the discrete transform, or decreasing the spacing between pixels. When this is done, the true nature of the scene becomes apparent in its pictorial representation.

To illustrate the resampling operation and to display the visual illusion in two dimensions, Figures 20-21 have been created. Figure 20 consists of rows of sinusoids extending from 0 cycles/pixel (cpp) at the top to 0.5 cpp (Nyquist frequency) in the center to 1.0 cpp at the bottom. Notice that the bottom half is the mirror image of the top half and that this is due to the aliasing of the entire bottom half of the image (the bottom half of the "scene" bears little resemblance to its image). Although the aliasing phenomenon is not the subject of this section, it is instructive to observe it in an image. Interference artifacts due to sampling of waves having frequencies greater than 0.25 cpp can be observed in the form of hyperbolae in the center and the four sides of the figure. These structures do not actually exist in the target even though they are readily observed in the image. An expansion of the image performed by simply replicating pixels produces no changes because the high frequencies are retained.

In Figure 21 the image was expanded by a factor of two by separating replicates in the discrete transform as described above. The image contains no waves with frequencies greater than 0.25 cpp, and the first-order interference artifacts have vanished. Furthermore, the image quality has not been degraded.

As a rule, to insure that digital images will be properly visually interpreted, it is necessary that the band-limited scene be sampled at a rate more than four or five times the band limit frequency. If this condition is not met during data acquisition, it may be achieved by properly resampling the image.

Some interference artifacts will remain until the pixel spacing is reduced to zero, which is the case for a continuous image. However, the strongest of these are removed by an image expansion of two times. Even this may be infeasible with the large images produced by current sensors because Fourier transforms must be computed. A compromise would seem to be interpolation using a cubic spline (Reference 15) or other function of finite size but performance superior to bilinear interpolation.

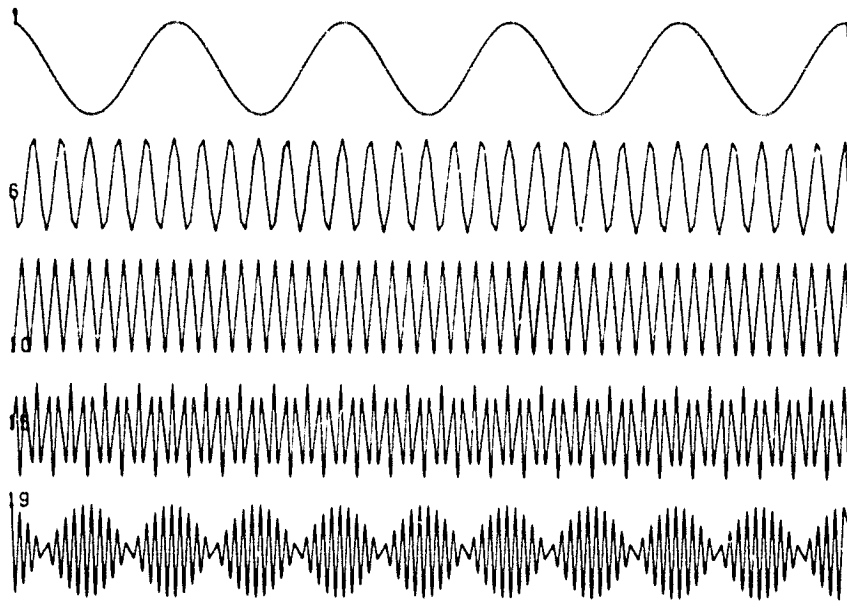


Figure 19. Sampled sinusoids showing interference effects of the sampling function. Samples have been connected by line segments for clarity. From top to bottom, wavelengths are 40, 40/6, 40/10, 40/15, and 40/19 samples.

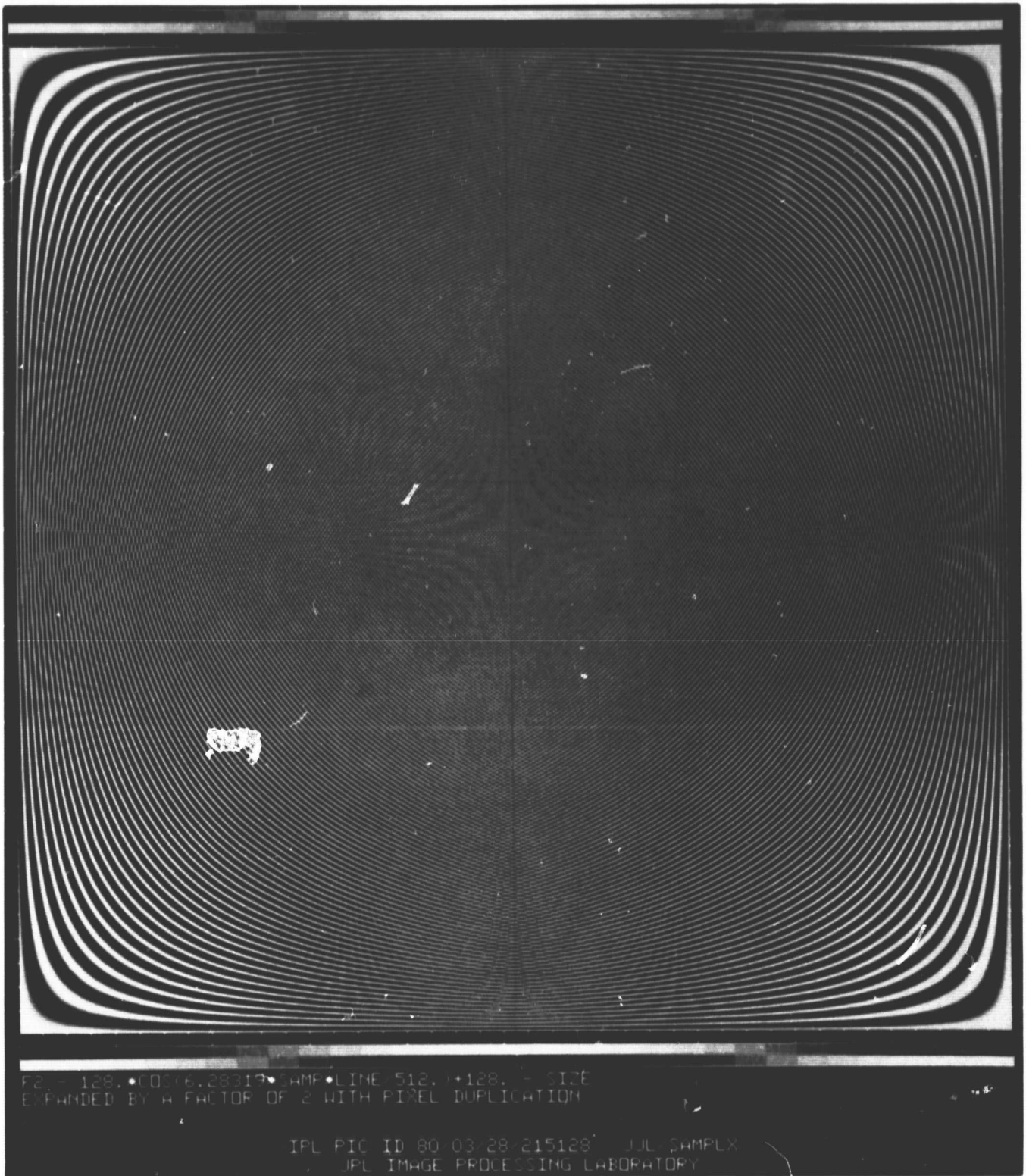


Figure 20. Sinusoid target showing interference patterns as hyperbolae at center and in central regions of the four edges. Each line in target is a sinusoid in the horizontal direction. Frequency changes in vertical direction from 0 at top line to 1 at bottom. Note mirror image caused by aliasing around the middle line (at the Nyquist frequency). Image size has been expanded by pixel replication.

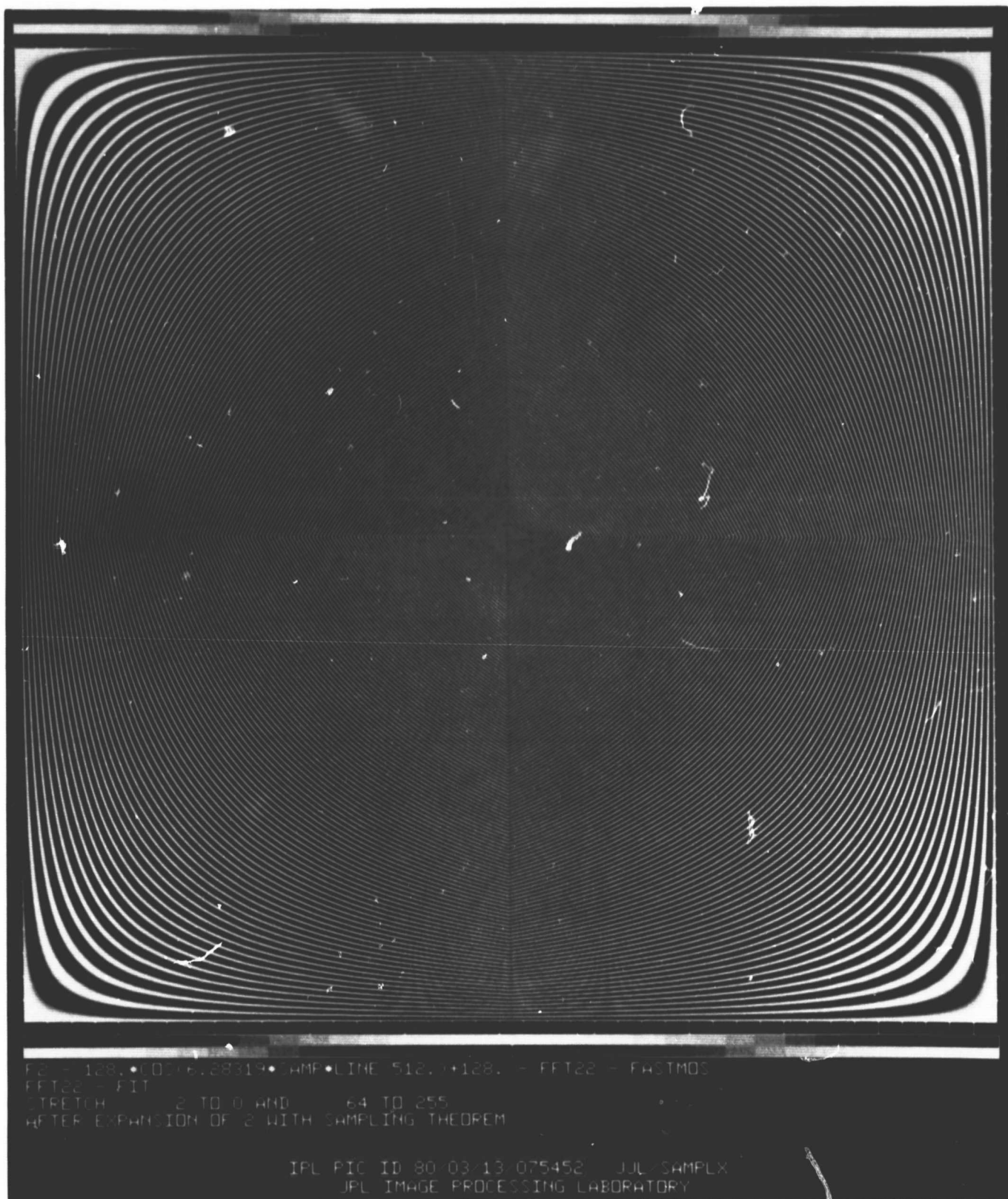


Figure 21. Sinusoidal target showing artifact suppression after twofold size expansion using the similarity theorem (sinc interpolation). The few artifacts remaining would be removed by further interpolation to create a more nearly continuous image. Contrast at high frequencies is preserved.

## SECTION XI

### LOW DYNAMIC RANGE INDUCED ILLUSIONS

Quantization of real and continuous scene brightness to integer values is a characteristic of all digital images. In the illustrations above, the quantization interval was  $2^7$  so that a sinusoid ranging in amplitude from -1 to +1 was encoded in 256 gray levels. In real scenes contrast may be reduced so that only a few quanta describe the range of amplitudes of a harmonic component of the image spectrum. This is commonly true for high frequency waves in unfiltered images, but may be true for any component in a filtered image. A problem can occur if the dynamic range of the sampled data is sufficiently narrow that integer truncation seriously modifies the true intensity values in the scene. In this event the quantized sinusoid is represented by a series of stacked square functions, or after sampling by the sum of truncated sequences of  $\delta$  functions. For instance, a sine wave of frequency 0.125 cpp which is quantized in two levels may be represented by the sequence (...-1, -1, -1, 0, 1, 1, 1, 0, -1, -1, -1, 0...). The Fourier transform of this sequence is not simply  $\delta(s + 0.125) + \delta(s - 0.125)$ , the transform of the sinusoid, but is instead the sum of the transforms of the three elementary sequences (0, 0, 0, -1, 0, 1, 0, 0...), (0, 0, -1, 0, 0, 0, 1, 0...), and (0, -1, 0, 0, 0, 0, 0, 1...), all of which are periodic with a wavelength of 8 samples and which add to produce the original sequence. The transform of these impulse pairs are themselves sinusoids having frequencies of 0.125, 0.25, and 0.375 cpp and the spectrum of the quantized sinusoid is

$$\sum_{n=1}^{\infty} \sin(2\pi n 0.125s) \quad (11)$$

In this example, if the spectrum were quantized at the same level as the image, each sinusoid in the spectrum would itself be a series of alternating impulses

$$\sum_{m=1}^3 \sum_{n=-\infty}^{\infty} (-1)^n \delta(s - 0.125 mn) \quad (12)$$

Thus harmonic overtones are created by the act of quantization, and these overtones may have frequencies exceeding the Nyquist frequency. In this case, the overtones will be aliased.

Figure 22 illustrates this phenomenon on a synthetic sinusoid image. The figure consists of four rows, each showing a sinusoid at the left, the log amplitude of the Fourier transform of this sinusoid to its right, and

a high-pass filter applied to the sinusoid at far right (after contrast enhancement). The difference between the four rows is in the dynamic range of the sinusoid. The frequency of the wave was controlled by populating a single element in an otherwise empty spectrum and inverse transforming into the function domain. The sinusoid thus created was then scaled to the different amplitude ranges shown in the left column of Figure 22. The Fourier transforms of the quantized sinusoids are reproduced in the center column and clearly show the presence of harmonic overtones.

Filtering of an image affected by this phenomenon may modify the amplitudes at the fundamental and overtone frequencies differently. To illustrate this, frequencies less than or equal to the fundamental frequency of the quantized sinusoid in Figure 22 were suppressed. The filtered images, shown in the right column of Figure 22, clearly show the presence of energy at overtone frequencies. In images of real scenes, this phenomenon must result most noticeably in an increase of high-frequency noise. However, all frequencies will be affected in an image dependent fashion, producing artifacts which are only indirectly related to the continuous scene.

Quantization artifacts cannot be removed from an image by filtering, except by also removing all fundamental energy at the same frequency. Resampling is likewise of no use. They are best minimized by selecting appropriate signal amplification prior to digital encoding. However, in any digital image some quantization artifacts will be found, and the analyst must anticipate encountering them during careful inspection of digital images.

Figure 22. Quantization artifacts in sinusoids. Left column shows sinusoidal targets. Center column shows their spectra. Although the target is a simple sine wave, overtones are present in the transforms. Right column shows filtered target with power at and below the fundamental frequency of the sine wave suppressed. In row 1 the sinusoid has a brightness range of  $2^3$  gray levels; in row 2 the target occupies  $2^4$  gray levels; in row 3 it occupies  $2^6$  gray levels; and in row 4 the brightness range is  $2^8$ . As the target contrast increases more overtones appear but the power at the fundamental frequency increases. For a continuous target an infinite number of overtones of zero amplitude would be present. Contrast in filtered images has been adjusted for display.



## SECTION XII

### SUMMARY AND CONCLUSIONS

Transformations of images into other coordinate systems provide two advantages: more information can be obtained from the image by simplifying the manner in which it is displayed. Algorithms designed to operate in one coordinate system can be induced to operate in virtually any geometry.

Simple operations such as division provide physical information on the M82 H $\alpha$  emission.

The Gull maximum entropy algorithm can be induced to provide greater resolution improvement without a visually disturbing increase in artifact.

Recovery of the amplitude from the phase of the Fourier transform of a maximum entropy restored image produces uncertain results. The process can be demonstrated on a noiseless target but may not be stable for practical imagery without the aid of other devices.

A technique was presented to select the most unique morphological types from a set of all observed types of galaxies.

It is possible to obtain approximate magnitudes automatically with a simple above-threshold search algorithm when variable nebulosity is present across the scene. This is accomplished by subtracting from the image a model of the local nebulosity produced with a median filter.

Relative color and polarization maps of R-Monocerotis indicate a dusty, hollow cone shaped reflection nebula illuminated by the star at its vertex.

Solid-state electronic cameras such as CCD's are prevented from sampling in accordance with the sampling theorem by their physical design. The principal consequence of this is undersampling and aliasing resulting in visual disruption of pictures of simple geometric targets or highly structured scenes. However, image filtering may reveal these effects even in images of ordinary scenes. Critical sampling or oversampling may be achieved by degrading the optics to produce a broad pointspread function, which band-limits the image projected onto the sensors.

Properly sampled scenes may be reconstructed by interpolation of the discrete images. This costly process is widely overlooked, resulting in the introduction of interference patterns in images. Again, simple geometric targets are most obviously affected, but filtered images of most scenes are adequately displayed by conventional means.

Quantization of image data necessarily introduces energy at harmonic overtones of the image spectrum. This energy is aliased if the frequency of the overtones exceeds 0.5 cycles/pixel. It cannot be selectively

removed from the image by filtering, and the best way to suppress it is to maximize the amplification of the sensor before digital encoding. The effect is reduced as the dynamic range is increased.

## REFERENCES

1. Lorre, J. J., Lynn, D. J., Application of Digital Image Processing Techniques to Astronomical Imagery - 1977, JPL Publication 78-17, Jet Propulsion Laboratory, Pasadena, CA, April 15, 1978.
2. Lorre, J. J., Application of Digital Image Processing Techniques to Astronomical Imagery - 1978, JPL Publication 78-91, Jet Propulsion Laboratory, Pasadena, CA, November 1, 1978.
3. Lorre, J. J., Application of Digital Image Processing Techniques to Astronomical Imagery - 1979, JPL Publication 79-109, Jet Propulsion Laboratory, Pasadena, CA, November 1, 1979.
4. Lorre, J. J., Enhancement of the Jets in NGC1097, ApJ, Vol. 222, No. 3, Part 2, L99-L103, June 15, 1978.
5. Morrison, P., Is M82 Really Exploding? Sky-Telescope, January 1979, pp. 26-31.
6. Vizvanathan, N., Sandage, A., Linear Polarization of the H $\alpha$  Emission Line in the Halo of M82 and the Radiation Mechanism of the Filaments, ApJ, Vol. 176, pp. 57-74, August 15, 1972.
7. Gull, S. F., Daniell, G. J., Image Reconstruction From Incomplete and Noisy Data, Nature, Vol. 272, No. 5655, pp. 686-690, April 20, 1978.
8. Fienup, J. R., Reconstruction of an Object from the Modulus of its Fourier Transform, Optics Letters, July 1978, Vol. 3, No. 1.
9. Siegal, B. S., Gillespie, A. R., Remote Sensing in Geology, Chapter 6, John Wiley & Sons, 1980.
10. Lorre, J. J., Gillespie, A. R., Artifacts in Digital Images, SPIE Conference on Application of Digital Image Processing to Astronomy #264, 1980, August 20, Caltech.
11. Goodman, J. W., Introduction to Fourier Optics, McGraw-Hill, p. 25, 1968.
12. Bracewell, R., The Fourier Transform and Its Applications, McGraw-Hill, p. 191, 1965.
13. Root, G., A Qualitative Study of the Trade-off Between Sample Spacing and MTF for Discrete Image Sensors, J.R. 900-631, Jet Propulsion Laboratory, California Institute of Technology, Pasadena, CA, 91103, 1973. (JPL internal document).
14. Linfoot, E. H., Fourier Methods in Optical Image Evaluation, Focal Press, p. 22, 1964.

15. Rifman, S. S., Digital Rectification of ERTS Multispectral Imagery, Symposium on Significant Results Obtained from Earth Resources Technology Satellite-1, NASA SP-327, pp. 1131-1142, National Aeronautics and Space Administration, Washington, D.C., 1973.